energies

MDPI

Article

Control of Cuk-Based Microinverter Topology with Energy Storage for Residential PV Applications

Yousef Alharbi and Ahmed Darwish *

School of Engineering, Lancaster University, Lancaster LA1 4YW, UK
* Correspondence: a.badawy@lancaster.ac.uk

Abstract: This paper proposes a modular inverter based on Cuk converters for solar photovoltaic (PV) systems to mitigate the voltage and current mismatch issue at the PV module level. The proposed modular Cuk inverter (MCI) is formed by connecting several low-voltage (LV) microinverters (MIs) in series and linking their output sides to the distribution network. This architecture does not require a central inverter, and hence, it eliminates the need for large dc-link intermediate capacitors. The proposed MCI provides more controllability over the PV system by having a decentralized structure. The MCI will improve the PV system efficiency by reducing the voltage and current stresses in the MIs and will enable better voltage regulation due to the provided controllability. Since the proposed MI topology is based on the Cuk converter, it offers continuous input and output currents that will reduce the required filtering capacitance and will provide a wide range of voltage regulation for either supplying the loads or charging the storage batteries. The paper presents the associated control scheme for the proposed MCI that employs two controlling loops. The input loop at the PV side is designed and tuned to eliminate the ripples from the input current, while the outer loop at the grid side will control the output ac current and hence the MCI power. Computer simulations are presented using MATLAB/SIMULINK software to examine the validity of the suggested inverter for distributed generation PV residential applications. A scaled-down experimental prototype controlled by TMS320F28335 DSP was built and used to validate the mathematical analyses and simulation results.

Keywords: photovoltaic (PV); power electronic converter; Cuk converter; switched mode power supply (SPMS); grid-connected systems

check for updates

Citation: Alharbi, Y.; Darwish, A. Control of Cuk-Based Microinverter Topology with Energy Storage for Residential PV Applications. *Energies* **2023**, *16*, 2293. https://doi.org/10.3390/en16052293

Academic Editors: Massimiliano Luna and Marcello Pucci

Received: 1 November 2022
Revised: 20 February 2023
Accepted: 23 February 2023
Published: 27 February 2023

Copyright: © 2023 by the authors. Licensee MDPI, Basel, Switzerland. This article is an open access article distributed under the terms and conditions of the Creative Commons Attribution (CC BY) license (https://creativecommons.org/licenses/by/4.0/).

1. Introduction

The energy crisis has led to an increased focus on renewable energy to meet the global electricity demand. Photovoltaic (PV) energy has become a major clean energy resource in the last few years due to the environmental and economic merits that it can provide [1]. PV systems are composed of PV cells, PV modules, PV panels, and PV arrays. According to the required power level, these components are usually connected in series to step up the output voltage and reduce the wiring cables' size between PV elements [2]. Improving the PV systems' efficiency and reducing their cost become important topics to promote them as a competitive energy source in the future [3]. Nevertheless, more effort is required to improve the efficiency of PV systems in order to compete with conventional energy sources [2,4].

Maximizing the PV system's efficiency can be achieved through different methods. One strategy for increasing the PV system efficiency is to operate the PV system at the maximum power point and apply the distributed maximum point tracking system at the PV module level [4,5]. The effect of the mismatch concerns due to non-equal voltage, current, and hence power, on small PV systems, is easier to consider compared with medium-scale and large PV systems. The mismatch issue might occur due to several reasons including partial shading (PS), PV panel orientation, and dust. The mismatch issue between PV

elements leads to different output power for each PV component. The mismatch between PV elements results in significant power loss or serious damage to the PV components [6]. Applying the distributed maximum power point tracking (MPPT) at the PV module level can result in effective utilization of the maximum output power from the PV system [7,8].

The solar PV cells are the building units of the PV module. The voltage of a single PV cell usually ranges from 0.5 to 1 volt according to the material used in the manufacturing process. The low voltage of the PV cell makes it less practical in most applications. Thus, the PV cells are connected in series to build up higher output voltages. The PV module is usually formed by connecting tens of PV cells in series. Nowadays, solar PV modules come in different sizes according to the number of cells in the PV module, which is usually between 60 and 72 PV cells [9]. The solar cells can be connected in a series of parallel combinations to form a photovoltaic cell array, and usually, this connection is integrated with bypass diodes to mitigate the partial shading effect [10].

The mismatch issue can lead to different power generations of PV elements, which means that each PV element operates at a unique maximum power point. The nature of the series connection of the PV elements means they share the same current; hence, when the mismatch exists, the whole PV system will be limited by the PV element with the lowest power generation [2]. The conventional strategy to overcome this issue is by connecting a bypass diode in parallel with each PV module, which might improve the PV system efficiency and solve hot spot concerns to some extent [2,9]. However, the power generated by the shaded PV module will be lost since the bypass diode will isolate it from the PV system [11].

Many strategies have been proposed to mitigate the mismatch issue and effectively utilize the maximum output power of the PV system [12]. Most of these methods find the optimal solution for the mismatch issue by operating each PV module at its individual maximum power point (MPP). One suggested solution for the mismatch problem is to link a DC–DC converter to the PV module and then operate at the MPP for each PV module individually [10]. This solution allows the extraction of the maximum power from each PV module, which significantly increases the power harvesting of the PV system. The PV system's efficiency is improved, and the voltage stress is reduced by up to 33%, allowing small and cost-effective components [11]. However, the efficiency of the PV system is limited by the efficiency of the converters [2].

The microinverter (MI) is another promising method to maximize the PV system efficiency and reduce the effect of partial shading and mismatch problems. This approach provides an individual DC–AC inverter for each PV module. The performance of the faulty PV module might be limited due to the mismatch problem, while the power production of the unshaded PV module will not be affected. The PV module DC–AC inverter can maximize energy harvesting of the PV system and mitigate the partial shading concern [13]. The installation and increasing the size of the PV system become relatively easier because of using MIs at the module level [14].

Designing the MIs is becoming a topic of interest for power electronic researchers due to the offered advantages including PV system cost reduction and its ability to achieve grid parity [15,16]. Such a technology can improve the PV system efficiency, increase the PV system reliability, and develop the overall PV system performance. In addition, the mismatch issue can be significantly reduced especially for rooftop PV applications [15]. Traditional DC–AC inverters suffer from poor conversion efficiency because it requires several power-processing stages. Moreover, it usually relies on Buck-boost converters where the input current is discontinuous, which might reduce the input power of the PV system [13]. Low-voltage MIs are a promising solution because of their capability to improve PV system efficiency for residential applications and some medium-scale PV projects. Recent studies have shown that power production might increase by more than 15% compared with string inverter PV systems. Unlike the string PV systems, the robustness of the PV system can be significantly improved, and the probability of the PV system failure becomes lower [16–18]. A three-phase isolated differential inverter based

on the SEPIC DC/DC converter has been presented in [19] with improved power quality and negative sequence harmonic component (NSHC) control. However, the work has not discussed the operation of the converter from the PV module perspective. The work in [20] discussed the operation of the differential Flyback three-phase inverter with parallel-connected inputs. Although the input current stresses are shared between the parallel PV modules and converters, the operation of the modular series-connected inverter has not been proposed. The work in [21] presented the series-connected modular inverter using cascaded H-bridge converters. Although the work presented the MPPT control system to extract the maximum energy from the PV module, the work has not discussed the effect of the discontinuous current from the H-bridge converters on the performance of the control system or the PV modules. The work also has not considered the second-order harmonic components in the case of single-phase operation.

This paper presents a new MI design to solve the mismatch problem caused by partial shading at the PV module level. The proposed modular Cuk inverter (MCI) is formed by connecting several MIs in series and linking their output sides to the distribution network. The MCI enables each PV module to harvest the maximum power since each one has an independent MPPT system. Usually, the PV module voltage can be relatively low, and accordingly, boosting up the voltage to meet the grid side voltage becomes a challenge; therefore, the proposed series-connected MI is beneficial. Selecting the Cuk inverter as the main MI will improve the performance of the system by keeping the input current constant with time. This means that small capacitors are required at the PV module sides, which will reduce the size and improve the reliability. One merit of the proposed MCI is that it does not require an extra decoupling circuit to decouple the DC power at the PV side from the grid side pulsating power. In this context, the paper presents the operation of the proposed MCI with the suitable control schemes to ensure the proper operation of the system when supplied from the PV module and also when integrated with the battery system that is necessary for energy storage in residential applications. The suggested MCI controller is constructed with two control loops to enhance the robustness of the design. The paper presents the mathematical analyses for the proposed system when it operates in different DC/AC and AC/DC modes during PV energy generation and charging and discharging the associated batteries. The performance of the proposed MCI is shown through experimental case studies using a 1 kW prototype controlled by a Texas Instruments TMS320F28335 digital signal processor (DSP).

The rest of the paper is constructed as follows: Section 2 presents the main configurations of residential PV systems; Section 3 explains the main modes of operations of the proposed MCI according to the required power flow; Section 4 explains the operation of the selected MI that forms the building block of the MCI in DC/DC, DC/AC, and AC/DC modes; Section 5 presents the models and controllers for the MIs; and Section 6 presents the operation of the proposed MCI and its control system. The final conclusions are summarized in Section 7.

2. Low-Voltage PV MI Configurations

The MIs can be connected at the output sides in either series or parallel configuration. The resultant two systems will be explained briefly in the following subsections.

2.1. Parallel-Connected PV MI

As shown in Figure 1a, each DC–AC MI can operate independently with respect to other MIs. Thus, the failure of one MI will not affect the others in the PV system. Usually, in residential PV systems, conventional MIs are required to boost the voltage from the PV side level at about 12~27 V DC to around 220~230 V-AC rms [15]. The high-voltage step-up ratio needed in this type to meet the output voltage of the grid side might adversely affect the PV system's efficiency and increase the installation cost [12,15].

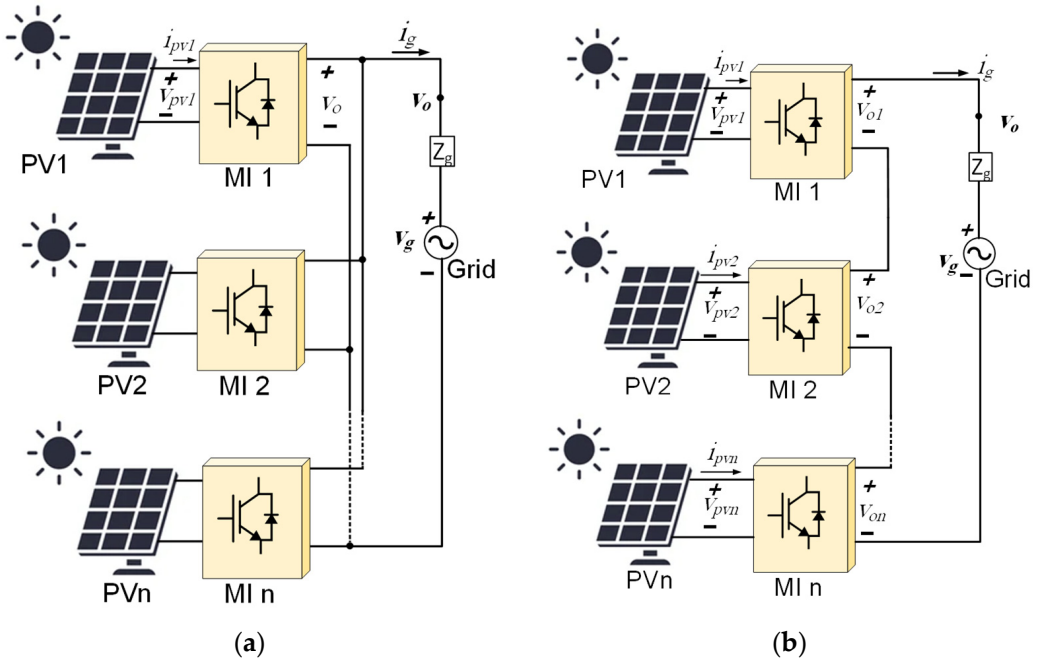


Figure 1. Low-voltage PV MI topologies: (**a**) Parallel-connected MI system and (**b**) series-connected MI system.

Using transformers with high turn ratios in parallel-connected ac module applications is common to meet the high voltage requirements at the grid side. However, this can increase the weight and the cost of the system. Therefore, transformer-less topologies and high-frequency transformers (HFTs) are suggested to mitigate this issue. Moreover, the non-isolated topologies of the PV applications with a high step-up ratio can increase the cost of the residential PV application due to increasing the size and the number of capacitors in the design. In terms of efficiency, the boost converters need to step the output voltage to a relatively high voltage, which can produce high-stress voltage to the switches and adversely affect the efficiency of the PV system [17].

2.2. Series-Connected PV MI

In a series-connected microinverter architecture, each low-voltage MI is connected to the adjacent one, and the series connection is tied to the grid. Figure 1b shows the connection of a series of MIs. In such a topology, the high step-up conversion ratio is not pressing because the series connection can meet the voltage requirements of the distribution network. In addition, the size of the magnetic elements and the stress voltage on the switches in the PV system can be significantly reduced. In contrast to the conventional low-voltage inverter, each MI is controlled independently, which increases the energy harvesting and improves the system's efficiency [17].

Because of these advantages, this paper is focused on the series-connected low-voltage PV MI system. In the proposed MCI architecture, shown in Figure 2, each MI is connected to the adjacent one. Employing the Cuk converter topology as an inverter for each PV module will obtain the maximum possible power from the PV panel and improve the system's efficiency. An independent MPPT algorithm is applied to each PV module, which can lead to solving the mismatch issue at the PV module level and increase the system harvesting. The configuration will benefit from the series connection to meet the voltage requirement at the grid side, and hence, providing a high step-up ratio is attainable.

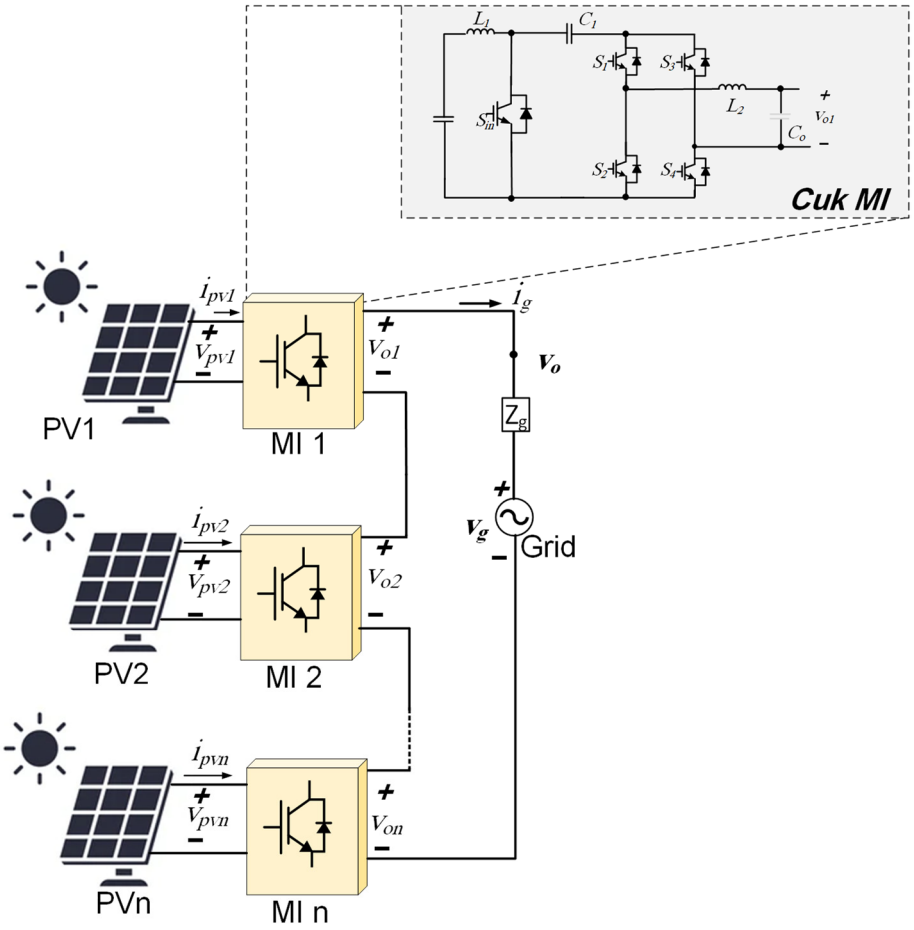


Figure 2. The proposed MCI.

2.3. System-Level Operation of the Series Connected System

As shown in Figure 2, the single-phase PV MCI system is connected to the grid through the grid impedance $Z_g = r_g + jL_g$, where r_g is the grid resistance and L_g is the grid inductance. The total voltage of the converter is the summation of the individual voltages of the series MIs. These total voltages v_o can be expressed as

$$v_o = V \sin(\omega t + \theta) \tag{1}$$

where V is the magnitude of the output voltage, θ is the phase shift with the grid voltage, and ω is the grid's angular frequency. V_g will be defined through the paper as the magnitude of the grid voltage. If the MIs supply active power P to the grid at a power factor cosφ, the values of V, θ, and the magnitude of the single-phase output current I_g can be expressed as

$$I_g = \frac{2P}{V_g \cos(\varphi)} \tag{2a}$$

$$\theta = \tan^{-1}\left[\frac{r_g I_g \sin(\varphi) + \omega L_g I_g \cos(\varphi)}{V_g + r_g I_g \cos(\varphi) - \omega L_g I_g \sin(\varphi)}\right] \tag{2b}$$

$$V = \left[\frac{V_g + r_g I_g \cos(\varphi) - \omega L_g I_g \sin(\varphi)}{\cos(\theta)}\right] \tag{2c}$$

In the normal operation, the MI number k in phase j generates the voltage of

$$v_{kj} = \frac{v_j}{n} \tag{3}$$

where n is the number of MIs.

3. General Modes of Operation

It is necessary for the modern residential energy sources to include energy storage systems (ESSs) to ensure that the extra energy during off-peak periods can be stored and used during the peak periods. The MCI can include individual battery packs with each MI as shown in Figure 3.

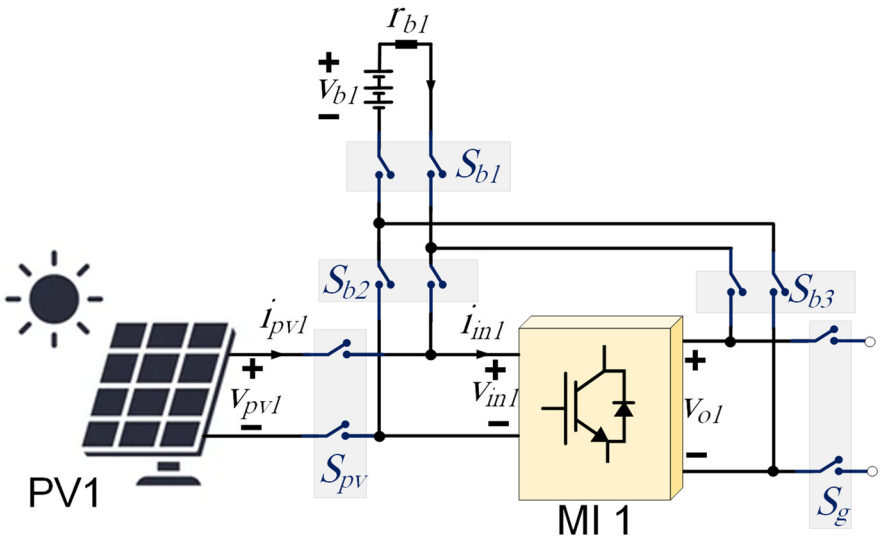


Figure 3. One MI of the proposed MCI with battery packs.

The proposed MCI can operate in four modes of operation depending on the connection of the relays as shown in Figure 4a, where each MI is associated with three single-pole-double-throw (SPDT) relays S_{pv}, S_{b1}, S_{b2}, and S_{b3}. These relays connect the MI to either the PV module, or the battery pack, or both. The output terminals of the MI are connected to the AC side via the output SPDT relay S_g. The four modes are detailed in the next subsections.

3.1. PV Modules to AC Grid

Figure 4a shows the operation when the power is delivered from the PV modules to the AC grid. All relays are opened except S_{pv} and S_g. In this mode, the active power P is determined by the maximum available power from the PV modules using the MPPT controllers. The voltages and currents are calculated as presented in (1) and (2). This mode is suitable for supporting the grid during the daytime when the PV modules generate their highest possible power. In this mode, the MCI is operating as a DC/AC inverter.

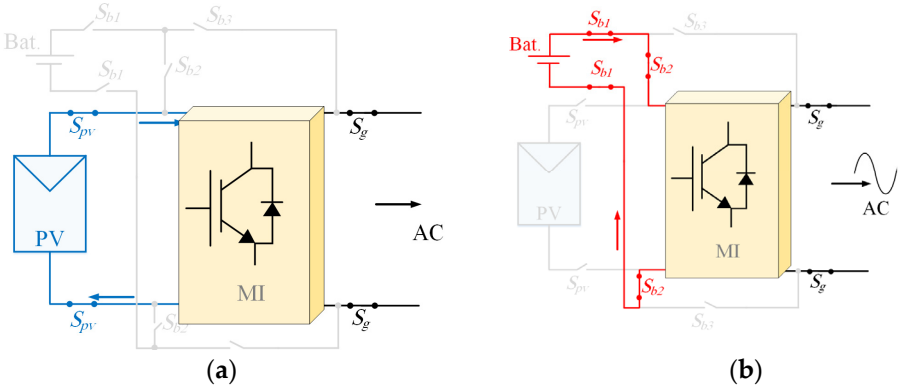


Figure 4. *Cont.*

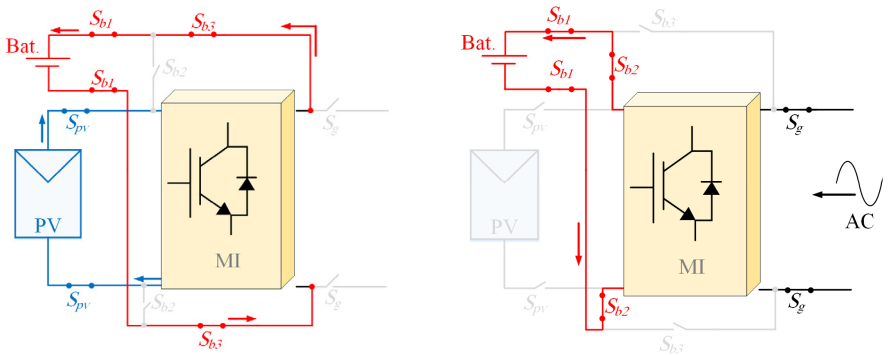


Figure 4. PV MCI with battery packs modes of operation: (**a**) DC/AC from PV to grid, (**b**) DC/AC from battery to grid, (**c**) DC/DC from PV module to battery, and (**d**) AC/DC from grid to battery.

3.2. Batteries Discharging into the AC Grid

If the PV modules power are not sufficient for grid support, the batteries can deliver the required energy by turning relays S_{b1} and S_{b2} on and turning relay S_{pv} off. Figure 4b shows the circuit in this case. The active power P is determined by the optimal discharge current from the battery to maximize its effective capacity and lifetime. In this mode, the MCI is still operating as a DC/AC inverter.

3.3. Batteries Charging from the PV Modules

If the AC grid does not need active power support from the PV modules at daytime, the batteries can be charged from the PV modules by connecting relays S_{b1} and S_{b3} with S_{pv} while disconnecting relay S_g as shown in Figure 4c. In this case, the power will be transferred from the PV modules to charge the batteries while the AC grid terminals are isolated. In this mode, the MCI is operating as a DC/DC converter.

3.4. Batteries Charging from the AC Grid

The batteries can be charged from the AC grid during the night with connecting relay S_g with S_{b1} and S_{b2} as shown in Figure 4d while all other relays are opened. In this mode, the MI is operating as an AC/DC rectifier, where the power is flowing from the grid side to the batteries through the MI.

4. The Operation of the Cuk MIs

To operate the MCI in the aforementioned modes, the selected MI must have specific features. First, it should be able to provide flexible voltage higher or lower than the input voltages from the PV modules, battery, or the grid. It should also provide isolation between the input and output side to meet the safety standards. This can be achieved if the selected MI enables the insertion of a high-frequency transformer (HFT). As the PV modules and the battery packs need to operate at constant voltages and current, the input current to the MI should be continuous and constant, while the output current and voltage are sinusoidal at the grid's 50/60 Hz. In other words, the MCI should be able to store the second-order voltage or current harmonics inside in suitable storage elements as shown in Figure 5.

For these reasons, the Cuk inverter shown in Figure 6 is the best candidate for the proposed modular system as it can achieve all the mentioned requirements [18]. The MCI consists of five semiconductor switches $S_1 \rightarrow S_5$, an isolating transformer with turns' ratio N_s/N_p, two inductors L_1 and L_2, two mandatory capacitors C_1 and C_2, and an optional capacitor C_o. The next subsections will present the modes of operation of the individual MIs and the modulation schemes during different modes.

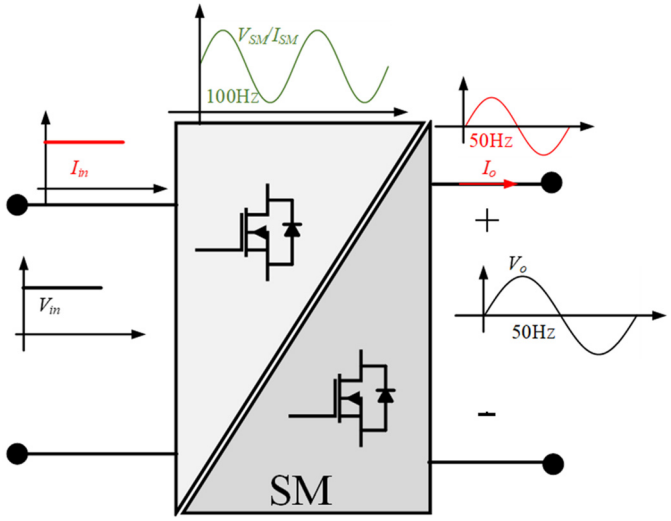


Figure 5. MCI inversion.

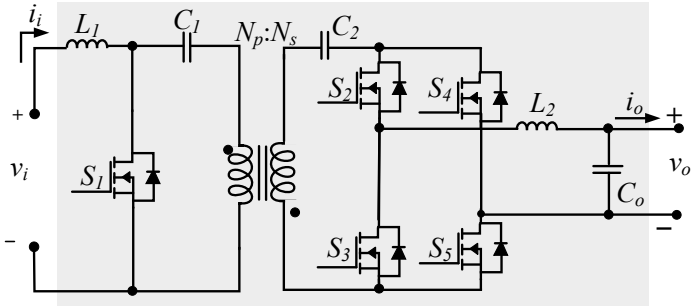
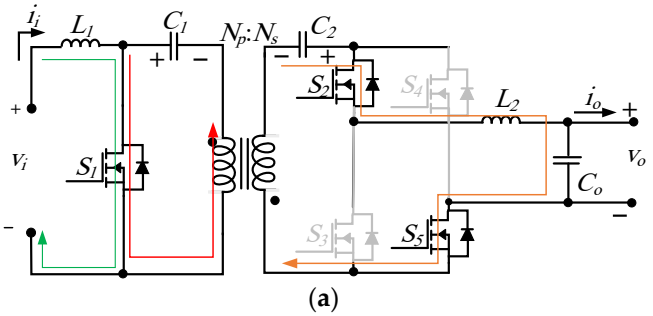


Figure 6. Cuk-based MI with isolation.

4.1. DC/DC Operation

The DC/DC operation will be required when the PV modules charge the associated battery packs. As shown in Figure 7, the MI operates in two states:

- During St_{dc1} ($0 \leq t < t_{on}$), switches S_1, S_2, and S_5 are turned on together. The input side current i_i is increasing to charge the inductor L_1. Meanwhile, the capacitors C_1 and C_2 are discharging in the output load leading L_2 to charge. The duration of this period is $t_{on} = dXt_s$, where d is the duty cycle ratio and t_s is the switching time of the MI. This state is shown in Figure 7a.
- During St_{dc2} ($t_{on} \leq t < t_s$), switch S_1 is turned off, and hence, the current i_i flows into the capacitors C_1 and C_2 leading them to charge. Switches S_3 and S_5 are turned on to provide a path for the current in L_2 to flow, and hence, the inductors' currents are decreasing. This state is shown in Figure 7b.



(**a**)

Figure 7. *Cont.*

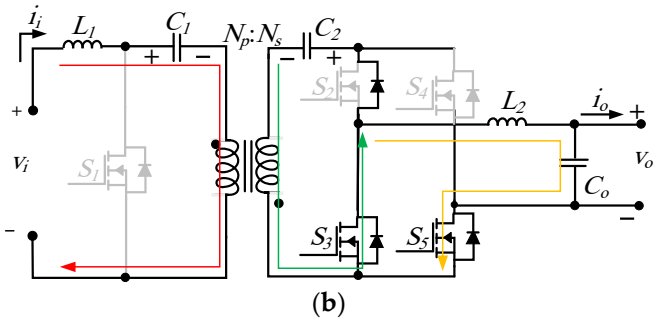


Figure 7. MCI as a DC/DC converter: (**a**) St_{dc1} and (**b**) St_{dc2}.

4.2. DC/AC Operation

The DC/AC operation with three states is activated when either the PV modules or the battery packs are supplying the grid with real power. When compared with the DC/DC mode, the additional state provides an extra degree of freedom to control the input and output sides together. This is necessary to keep the input current constant while generating sinusoidal output voltages and current as presented earlier in Figure 5. The three states are shown in Figure 6 and can be explained as follows:

- During St_{inv1} ($0 \leq t < t_{on1}$), switch S_1 is turned on so the input current i_i increases and L_1 is charged. The capacitors C_1 and C_2 discharge in the output load through S_2 and S_5 if i_o is in its positive half cycle and through S_3 and S_4 if i_o is negative. As shown in Figure 8a, L_2 is charged in this state. The duration of this state is $t_{on1} = d_1.t_s$.
- During St_{inv2} ($t_{on1} \leq t < t_{on1} + t_{on2}$), switch S_1 is still on. However, the capacitors C_1 and C_2 are charged by turning S_3 and S_4 on in the positive half cycle of i_o or by turning switches S_2 and S_5 on in the negative half cycle. In this case, L_2 is charged while L_1 is still charging. Therefore, this state provides the decoupling between the input and output sides as shown in Figure 8b. The duration of this state is $t_{on2} = d_2.t_s$.
- During St_{inv3} ($t_{on1} + t_{on2} \leq t < t_s$), switch S_1 is turned off, and therefore, capacitors C_1 and C_2 are still charged by turning but with the input current i_i. If i_o is in its positive half cycle, S_3 and S_5 will be turned on to provide a path for the current in L_2 to flow, and hence, the inductors' currents are decreasing (see Figure 8c). The same case will occur in the i_o negative half cycle when using switches S_2 and S_4.

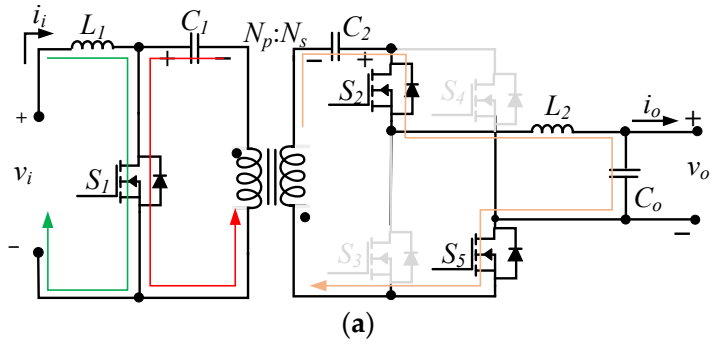


Figure 8. *Cont.*

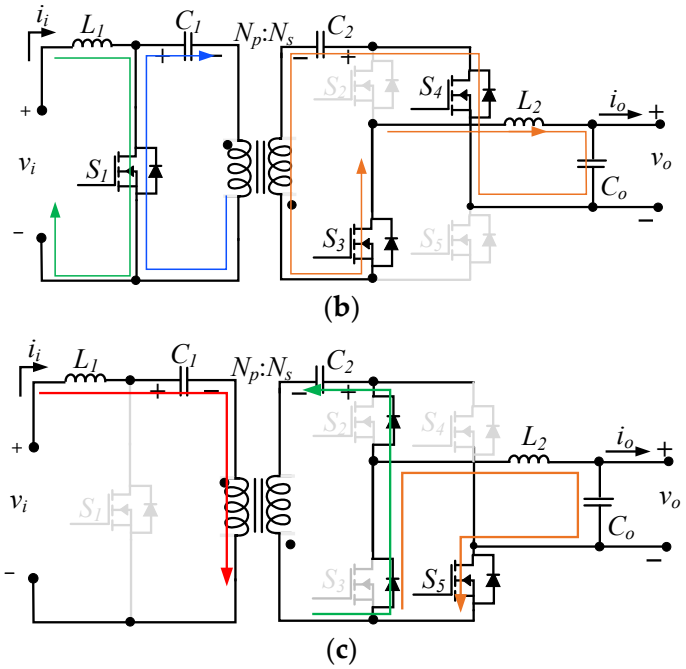


Figure 8. MCI as a DC/AC inverter when i_o is positive: (**a**) St_{inv1}, (**b**) St_{inv2}, and (**c**) St_{inv3}.

4.3. AC/DC Operation

The MCI will operate as an AC/DC rectifier when it is required to charge the battery packs from the AC grid. Similar to the inverter operation, the additional state in the modulation scheme provides an additional degree of freedom to control the input grid current and output battery pack's current independently. This will keep the battery pack's current constant with time. The three states are shown in Figure 7 and can be explained as follows:

- During St_{rec1} ($0 \leq t < t_{on1}$), switch S_1 is turned off so the battery current i_i increases and L_1 is charged. The capacitors C_1 and C_2 discharge in the battery through S_2 and S_3. The grid side current charges through S_3 and S_5 or through S_2 and S_4. As shown in Figure 9a, L_2 is charged in this state. The duration of this state is $t_{on1} = d_1.t_s$.
- During St_{rec2} ($t_{on1} \leq t < t_{on1} + t_{on2}$), switch S_1 is turned on, and hence, the battery's current will decrease. Meanwhile, capacitors C_1 and C_2 are discharged by turning S_3 and S_4 as shown in Figure 9b. The grid's side current is increasing while the battery's current is decreasing in this state. The duration of this state is $t_{on2} = d_2.t_s$.
- During St_{rec3} ($t_{on1} + t_{on2} \leq t < t_s$), switch S_1 is still turned on, and hence, the battery's current is decreasing. The capacitors C_1 and C_2 are charged by turning all the other switches off, and hence, the grid current is commutating in the diodes of S_2 and S_5. In this case, both inductors L_1 and L_2 are discharging, and their currents decrease as shown in Figure 9c.

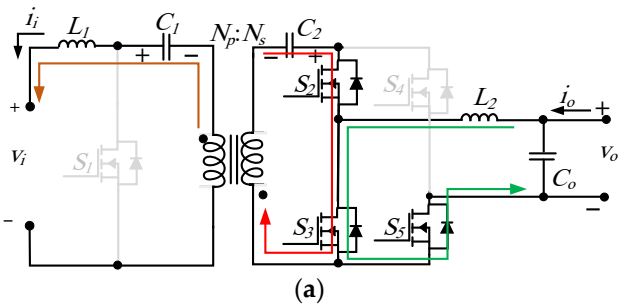


Figure 9. *Cont.*

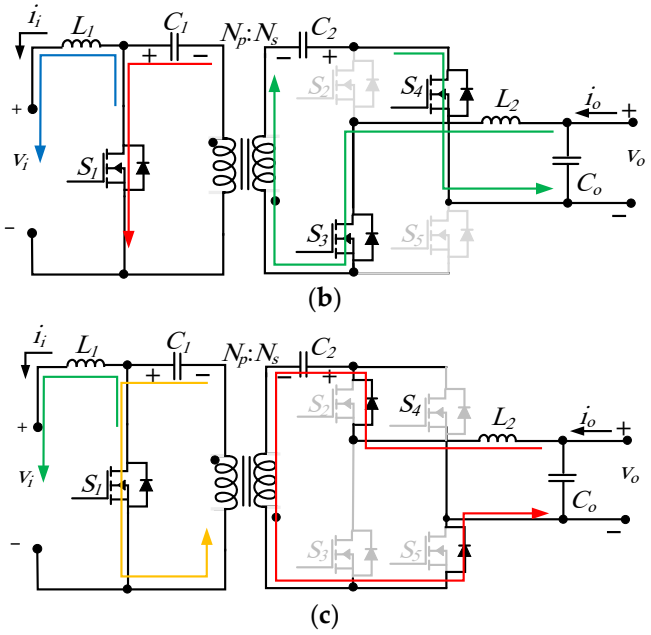


Figure 9. Cuk MI as an AC/DC rectifier when i_o is positive: (**a**) St_{rec1}, (**b**) St_{rec2}, and (**c**) St_{rec3}.

5. MI Modelling and Control

As explained in the previous subsections, the MI operates in three states except for the DC/DC operation. Thus, the state–space model will be obtained by averaging the three states along t_s. More details about the averaging method can be found in [22–24].

5.1. DC/AC Model (from PV Modules/Batteries into AC Grid)

The state vector can be expressed as $x(t) = [i_i(t)\ v_{Ct}(t)\ i_{L2}\ (t)\ v_o(t)\ i_o\ (t)]$ and the output $y(t) = i_g(t)$ is the grid current. i_i(t) is the input current, v_o(t) is the output voltage, i_{L2}(t) is the output inductor's current, and i_o(t) is the MI output current. The state $v_{Ct}(t)$ is expressed as $Nv_{C1}(t) + v_{C2}(t)$, N is the turns ratio (N_s/N_p), and C_t is $C_1C_2/(C_1 + N^2C_2)$. The average model is deduced in (4).

$$\dot{x}(t) = A_{inv}x(t)_. + B_{inv}\begin{bmatrix} v_i \\ v_g \end{bmatrix}$$

$$A_{inv} = \begin{bmatrix} 0 & \frac{d_1+d_2-1}{NL_1} & 0 & 0 & 0 \\ \frac{1-d_1-d_2}{NC_t} & 0 & \frac{d_2-d_1}{NC_t} & 0 & 0 \\ 0 & \frac{d_1-d_2}{L_2} & 0 & \frac{-1}{L_2} & 0 \\ 0 & 0 & \frac{1}{C_o} & 0 & \frac{-1}{C_o} \\ 0 & 0 & 0 & \frac{1}{nL_g} & 0 \end{bmatrix}_. \quad B_{inv} = \begin{bmatrix} \frac{1}{L_2} & 0 \\ 0 & 0 \\ 0 & 0 \\ 0 & 0 \\ 0 & \frac{-1}{L_g} \end{bmatrix} \tag{4}$$

The transfer function of the inverter is

$$G_{inv}(s) = \frac{i_o}{V_i} = C_{inv}(sI - A_{inv})^{-1}B_{inv}$$
$$C_{inv} = [\ 0 \quad 0 \quad 0 \quad 0 \quad 1\ ] \tag{5}$$

Figure 10 shows the PV module-level control when the MCI is operating as a single-phase inverter and the power flows from the PV modules to the ac grid. The reference input current i_i* is calculated from the MPPT controller, and then the actual current is controlled by a simple hysteresis controller. The output current is controlled by another proportional-resonant (PR) controller tuned at the grid frequency $\omega_o = 2\pi f$. It should be noted that this control system assumes that all the PV modules operate at the same irradiance and other weather conditions. However, another system-level control will be necessary in case of

partial shading to distribute the power on the MIs according to their different maximum power points.

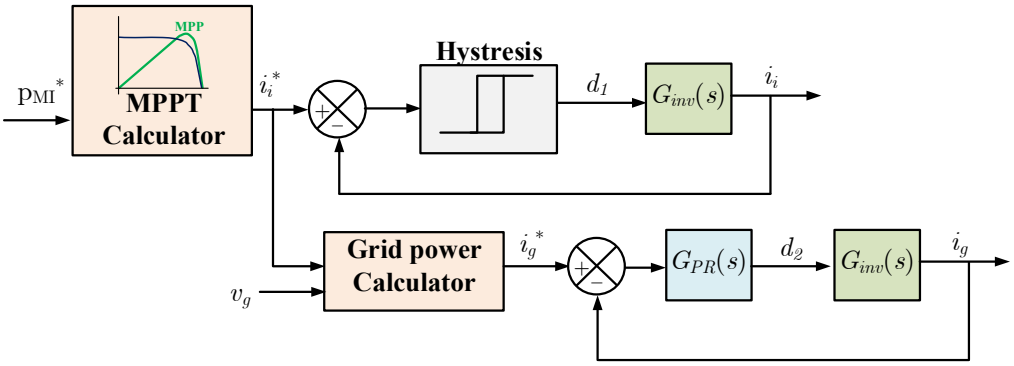


Figure 10. MCI controller during DC/AC inversion from PV modules to grid.

Figure 11 shows the module-level control when the MCI is still operating as a single-phase inverter but with the power flowing from the battery packs to the ac grid. There is no maximum power point to operate at in this case, and therefore, the batteries' discharging currents are flexible. However, the reference current may be chosen according to the batteries' nominal current value recommended by the manufacturer to maximize their lifetime.

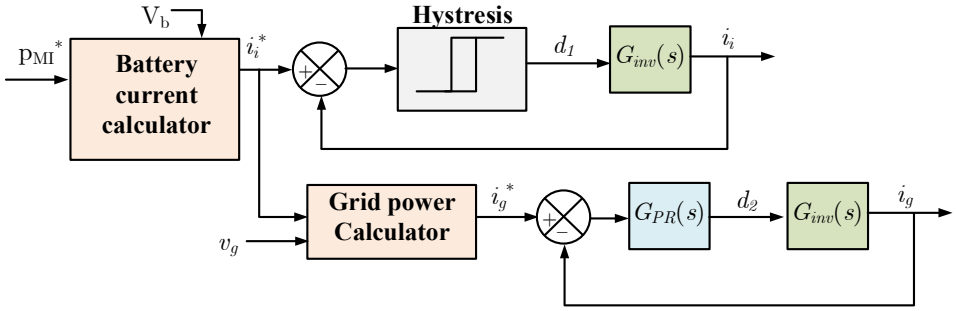


Figure 11. MCI controller during DC/AC inversion from battery packs to grid.

5.2. AC/DC Model (from AC Grid to Battery Packs)

The state vector of the AC/DC operation can be expressed as $x_{rec}(t) = [i_o\ (t)\ i_{L2}\ (t)\ v_o(t)\ v_{Ct}(t)\ i_i(t)]$, and the output $y_{rec}(t) = i_i(t)$ is the battery current. The average model is expressed in (6).

$$\dot{x}(t) = A_{rec}x(t)_. + B_{rec}\begin{bmatrix} v_i \\ v_g \end{bmatrix}$$
$$A_{rec} = \begin{bmatrix} 0 & 0 & \frac{-n}{L_g} & 0 & 0 \\ 0 & 0 & \frac{1}{nL_2} & \frac{1-d_1}{L_2} & 0 \\ \frac{1}{C_o} & \frac{-1}{C_o} & 0 & 0 & 0 \\ \frac{1-2d_2-d_1}{C_t} & 0 & 0 & 0 & \frac{-d_1}{NC_t} \\ 0 & 0 & 0 & \frac{d_1}{NL_1} & 0 \end{bmatrix}. \quad B_{rec} = \begin{bmatrix} 0 & \frac{1}{L_g} \\ 0 & 0 \\ 0 & 0 \\ 0 & 0 \\ \frac{-1}{L_1} & 0 \end{bmatrix} \tag{6}$$

The transfer function of the rectifier is

$$G_{rec}(s) = \frac{i_i}{V_g} = C_{rec}(sI - A_{rec})^{-1}B_{rec}$$
$$C_{rec} = [\ 0\ \ 0\ \ 0\ \ 0\ \ 1\ ] \tag{7}$$

Figure 12 shows the PV module-level control when the MCI is operating as a single-phase rectifier to charge the battery packs from the AC grid. Based on the reference MI

power p_{MI*}, the reference grid current $i_o{}^*$ is calculated using the grid power calculations, and then the actual current is controlled by a PR controller. The battery's reference current $i_i{}^*$ is calculated by estimating the battery's voltage as well as the state of charge and then controlled by a hysteresis controller.

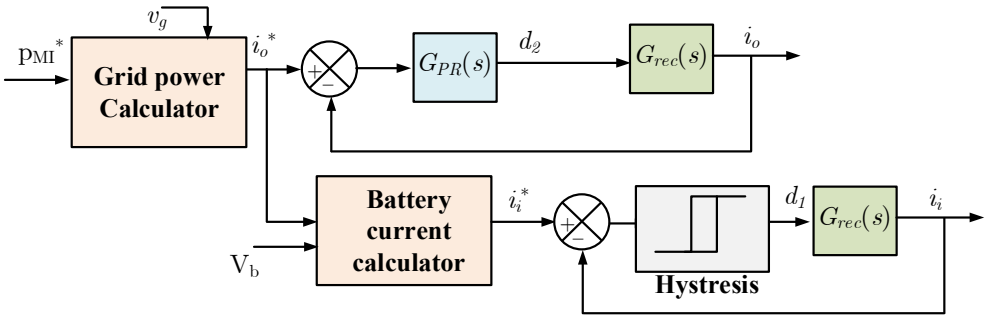


Figure 12. MCI controller during AC/DC conversion to charge the battery.

5.3. DC/DC Model (from PV Modules to Battery Packs)

The state vector of the MI in this case can be expressed as $x_{dc}(t) = [i_i(t)\ v_{Ct}(t)\ i_{L2}\ (t)\ v_o(t)\ i_o\ (t)]$, and the output $y_{dc}(t) = i_i(t)$ is the battery current. The average model is deduced in (8).

$$\dot{x}(t) = A_{dc}x(t) + B_{dc}\begin{bmatrix} v_i \\ v_b \end{bmatrix}$$
$$A_{dc} = \begin{bmatrix} 0 & \frac{1-d}{NL_1} & 0 & 0 & 0 \\ \frac{1-d}{NC_t} & 0 & 0 & 0 & \frac{-d}{C_t} \\ 0 & \frac{-d}{L_2} & 0 & \frac{-1}{L_2} & 0 \\ 0 & 0 & \frac{1}{C_o} & 0 & \frac{-1}{C_o} \\ 0 & 0 & 0 & \frac{1}{L_2} & 0 \end{bmatrix} B_{dc} = \begin{bmatrix} \frac{1}{L_1} & 0 \\ 0 & 0 \\ 0 & 0 \\ 0 & 0 \\ 0 & \frac{-1}{L_2} \end{bmatrix} \quad (8)$$

The transfer function of the converter is

$$G_{dc}(s) = \frac{i_o}{V_i} = C_{dc}(sI - A_{dc})^{-1}B_{dc}$$
$$C_{dc} = [\ 0\ \ 0\ \ 0\ \ 0\ \ 1\ ] \quad (9)$$

Figure 13 shows the controller for charging the batteries from the PV modules through the MIs. The reference input current $i_i{}^*$ is calculated from the MPPT controller and then the actual current is controlled by a simple hysteresis controller. For simplicity, the battery's output current is left uncontrolled assuming that the PV power will not exceed the rated power of the MI and the battery pack.

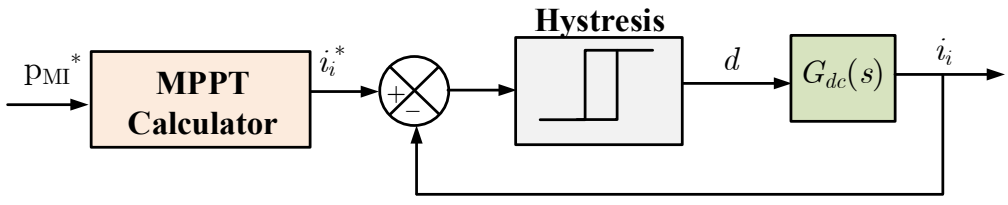


Figure 13. MI controller during DC/DC conversion to charge the battery.

6. MCI Operational Case Studies

Figure 14 shows the experimental setup for the MCI, which was controlled by a TMS32028335 DSP with the parameters in Table 1. The DC voltage sources were used to mimic the PV modules in the associated modes of operation. Each MI was connected to a battery segment composed of 12 series lithium-ion battery cells at approximately 50 V. The battery packs are shown in Figure 15. To ensure the safety of the prototype, the battery packs were controlled by the EMUS battery management system (BMS), which

continuously monitored the voltage, temperature, and current of each cell using a dedicated cell module circuit.

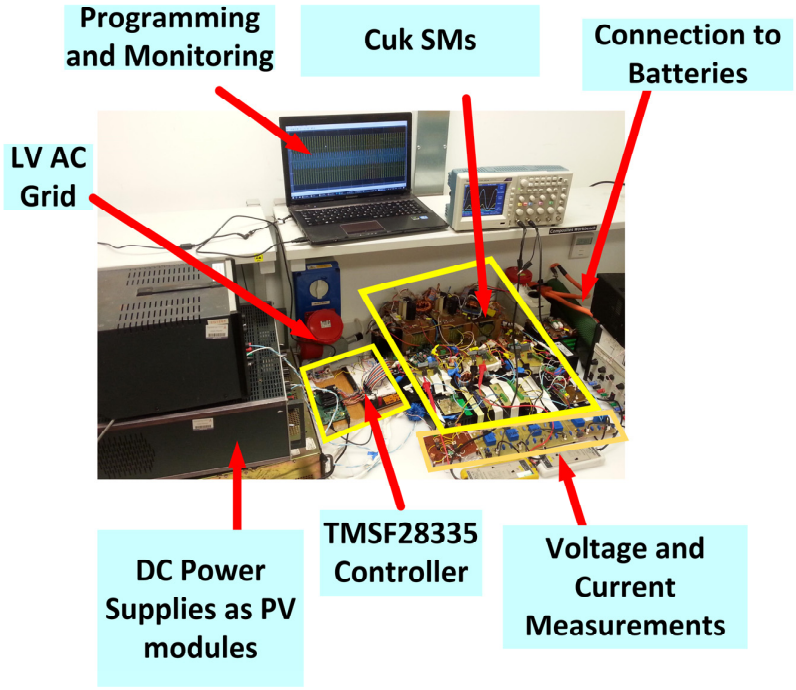


Figure 14. MCI experimental prototype.

Table 1. Parameters of the MCI model.

Parameters	Value
Number of modules	$n = 4$
MI rated power	$p_{MI} = 250$ W
MI inductors	$L_1 = L_2 = 0.5$ mH
MI capacitors	$C_1 = C_2 = 80$ µF—$C_o = 1$ µF
MI Switching frequency	$f_s = 50$ kHz
Transformer turns' ratio	$N = 1$
Charged battery voltage	$V_{bat} = 12$ s $\times$ 4.1 V $\approx$ 49 V
Grid voltage	325 V peak
Grid impedance	$L_g = 1$ mH, $r_g = 0.5$ Ω
Grid frequency	$f = 50$ Hz

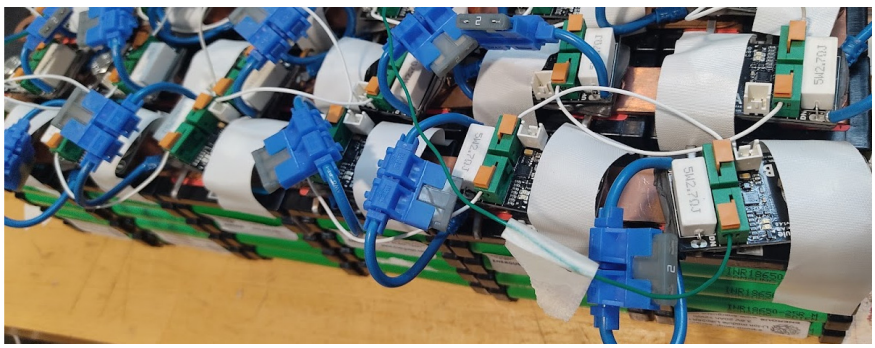


Figure 15. Battery segments.

The cell modules transferred their voltage, current, and temperature measurements to the central controller using the Controller Area Network (CAN) communication bus. The next subsections will present experimental case studies to explore the operation of the proposed MCI.

6.1. DC/AC Model (from PV Modules into AC Grid)

Figure 16 shows the full system with the PV module and system-level controllers. The MPPT algorithm itself is not in the scope of this paper, and therefore, it will be assumed that the reference power values for each PV module are already known and calculated. The reference current of the k_{th} MI was controlled by the duty-cycle ratio d_{1k}. The other duty-cycle ratio d_{2k} controlled the output voltage and current using the PR controller. The gains of the PR controller are defined as k_p and k_r. d_{1k} and d_{2k} for different MIs were not identical if the MIs had different operational points for any mismatch such as partial shading, for example. These individual MI controllers operated the system properly if all MIs were at identical operational points. However, a system-level controller was necessary in the case of mismatch to balance the output voltages and current of the different MIs. The system-level controller at the top right generated a central duty-cycle ratio D_2 for all MIs, which was added to the individual d_{2k} duty-cycle ratios. Figure 17 shows the power command for the MCI system. During the period T_1, MCI had equal power sharing between the four MIs when they started from zero power and increased gradually. During T_2, the MIs reached the maximum power of 250 W. The period T_3 simulated the partial shading when the top two MIs kept generating 250 W, while the other two dropped to 30%, causing the total power to decrease to 65%.

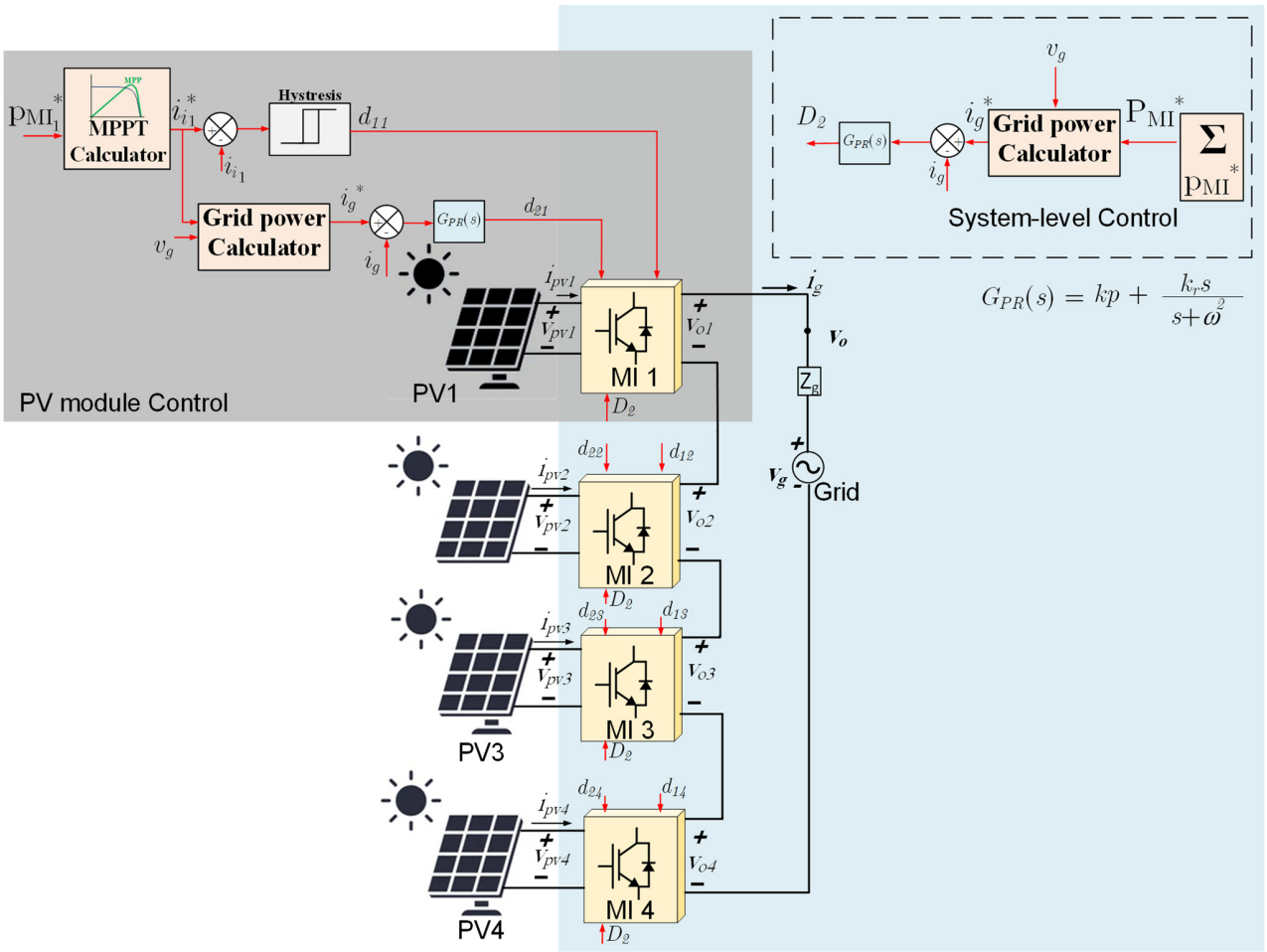


Figure 16. MCI, PV module, and system-level controllers for PV/grid DC/AC inversion.

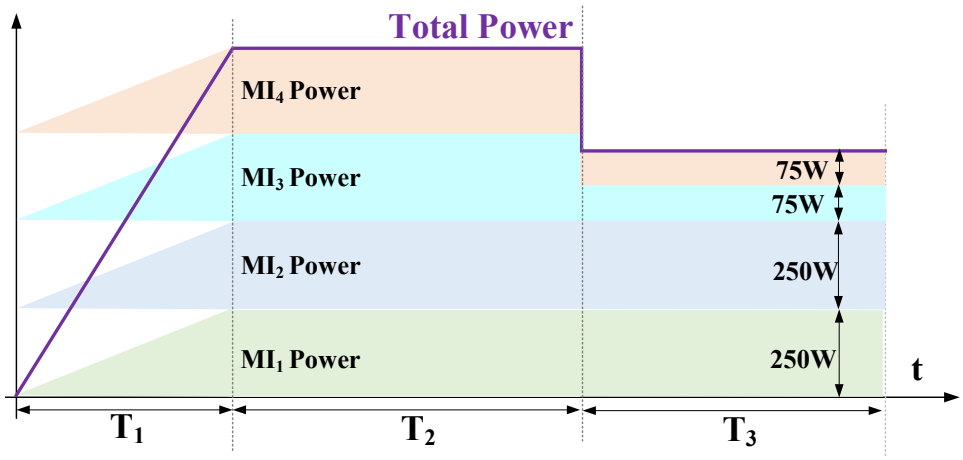
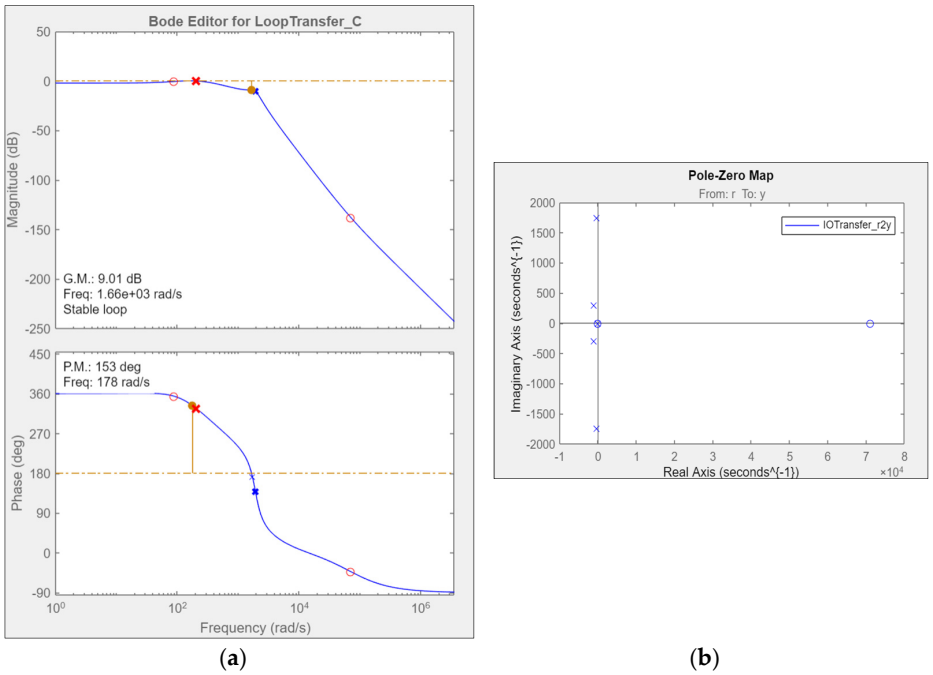


Figure 17. Power distribution of the four MIs during PV to grid DC/AC inversion.

The Sisotool® toolbox in MATLAB/SIMULINK was used to tune the PR transfer function's gains in order to compromise between the stability and the bandwidth, as shown in Figure 18. The decentralized control obtained the maximum available power during each interval, as shown in Figure 19. The real power was controlled to a good extent as shown in Figure 19a, where the power increased from 0 W to 250 W for all MIs. Then at t = 0.3 s, the MI_3 and MI_4 powers dropped to 30% to simulate the partial shading conditions. Because the input side of each MI was controlled by d_{1k} while the output side was controlled by $d_{2k} + D_2$, the input currents were kept constant with time, which means that the second-order power was stored in the flying capacitors. The grid voltage with the output grid current is shown in Figure 19b, where the current followed the power directly. The output voltages of the MIs were equal when the individual MIs powers were equal. During the partial shading conditions, the MIs with higher powers generated higher voltages because all MIs shared the same output current. The output voltages of the MIs are shown in Figure 19c. The input voltages of the power supplies used to mimic the PV module voltages are shown together in Figure 19d.



(**a**) (**b**)

Figure 18. Control loops during the PV to grid inversion: k_p = 2.5 and k_r = 5. (**a**) Bode plot. (**b**) Pole-zero map.

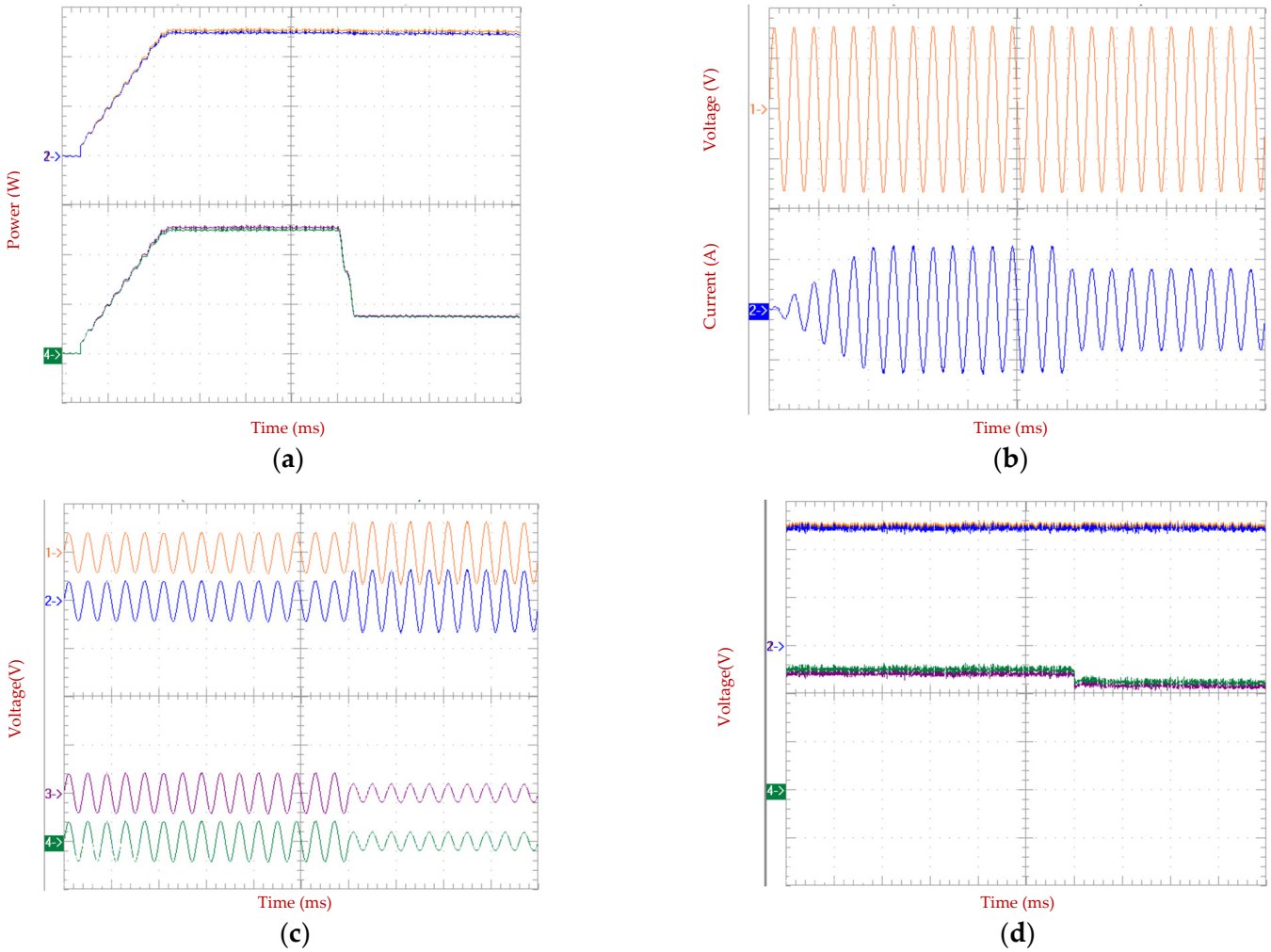


Figure 19. Experimental results of the MIs during PV to grid DC/AC inversion. (**a**) Powers: top (Ch1 and Ch2), MI_1 and MI_2; bottom (Ch3 and Ch4), MI_3 and MI_4; 50 ms/div–100 W/div. (**b**) Top (Ch1), grid voltage at PCC; bottom (Ch2), grid current; 50 ms/div–200 V/div–5 A/div. (**c**) Output voltages: top (Ch1 and Ch2), MI_1 and MI_2; bottom (Ch3 and Ch4), MI_3 and MI_4; 50 ms/div–200 V/div. (**d**) Input (power supplies) voltages: top (Ch1 and Ch2), MI_1 and MI_2; bottom (Ch3 and Ch4), MI_3 and MI_4; 50 ms/div–20 V/div.

6.2. Battery Packs vs. AC Grid

The control system to discharge the battery packs into the AC grid is shown in Figure 20. It was similar to the PV/grid controller but without the MPPT controller as the batteries did not have a maximum power point. The charging control system is shown in Figure 21, where the MCI system operated as a rectifier when the power command reversed its direction. Figure 22 shows the case study of discharging and then charging the battery pack.

Between t = 0 and t = 0.1 s, the battery packs were discharged gradually into the AC grid until each MI reached 100% of the rated value, which was 250 W. At t = 0.3 s, the power command was reversed, and the battery packs were charged at 25%. Figure 22a shows the powers of each MI. Figure 22b shows the grid current. Figure 22c shows the terminal ac voltage of each MI. Figure 22d shows the battery terminal voltages during discharging and charging.

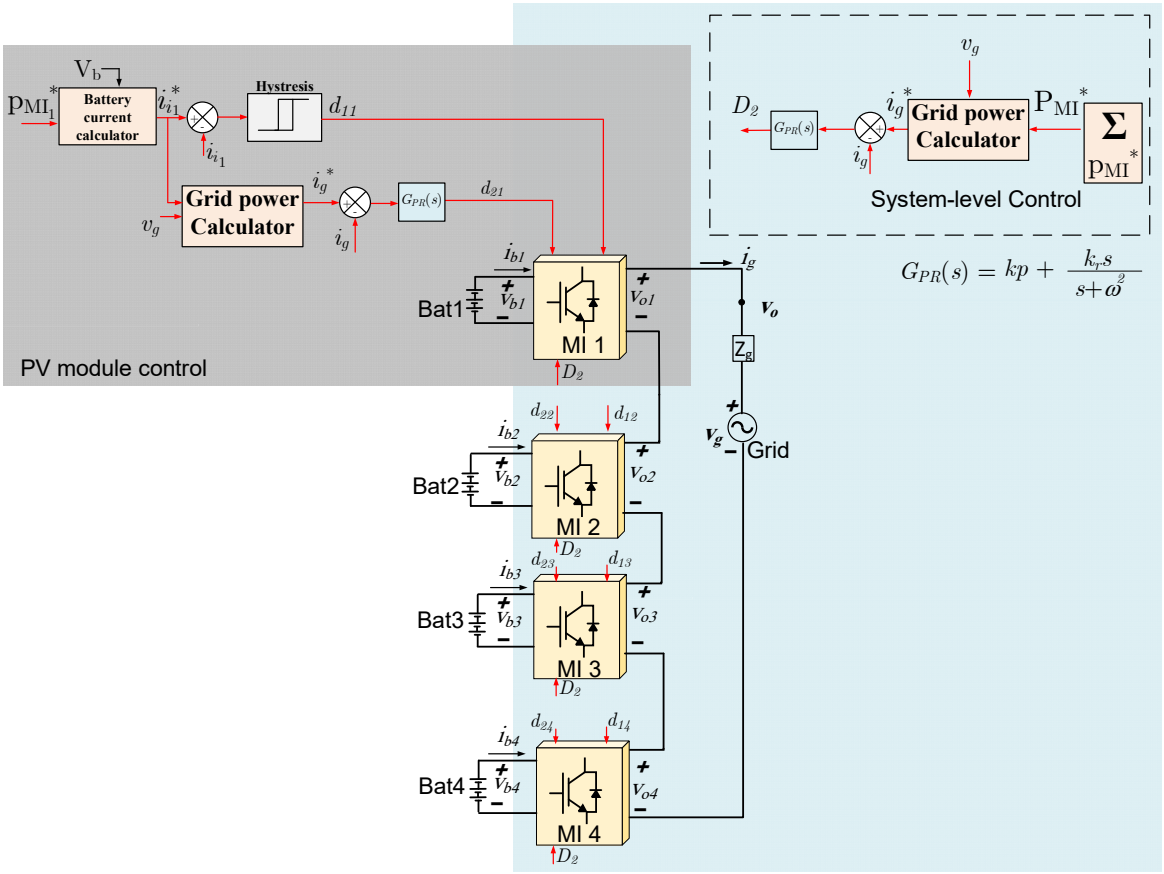


Figure 20. PV module and system-level controllers for battery/grid DC/AC inversion.

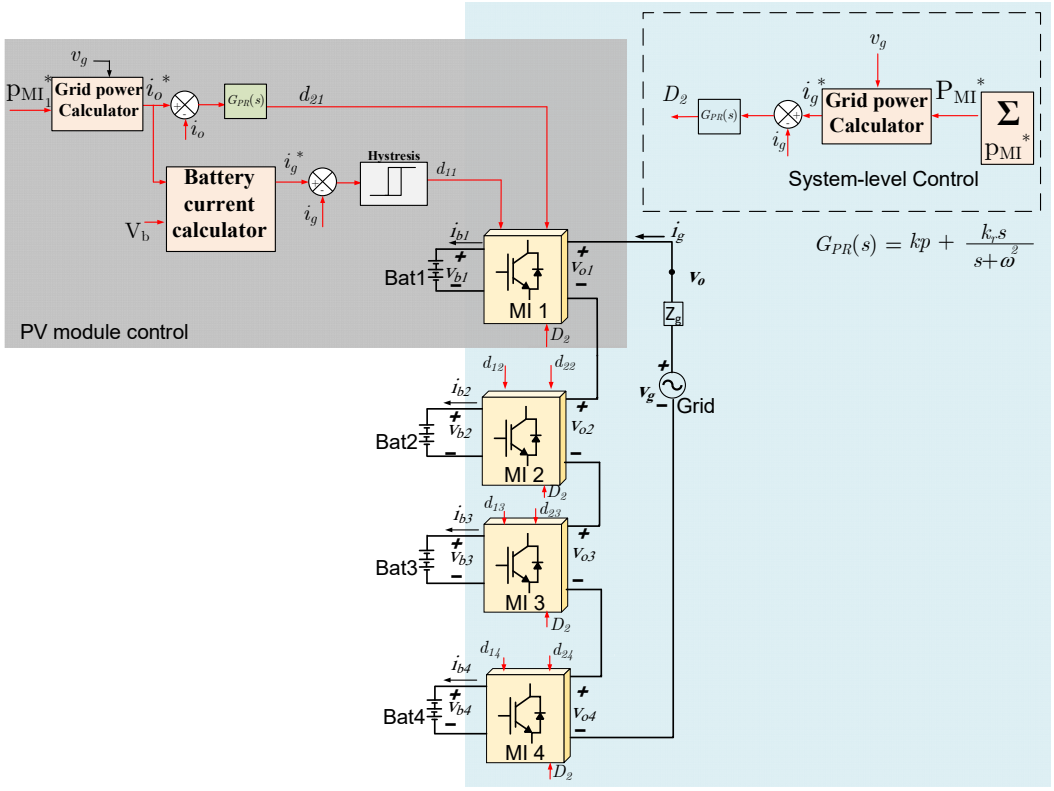


Figure 21. PV module and system-level controllers for grid/battery AC/DC rectification.

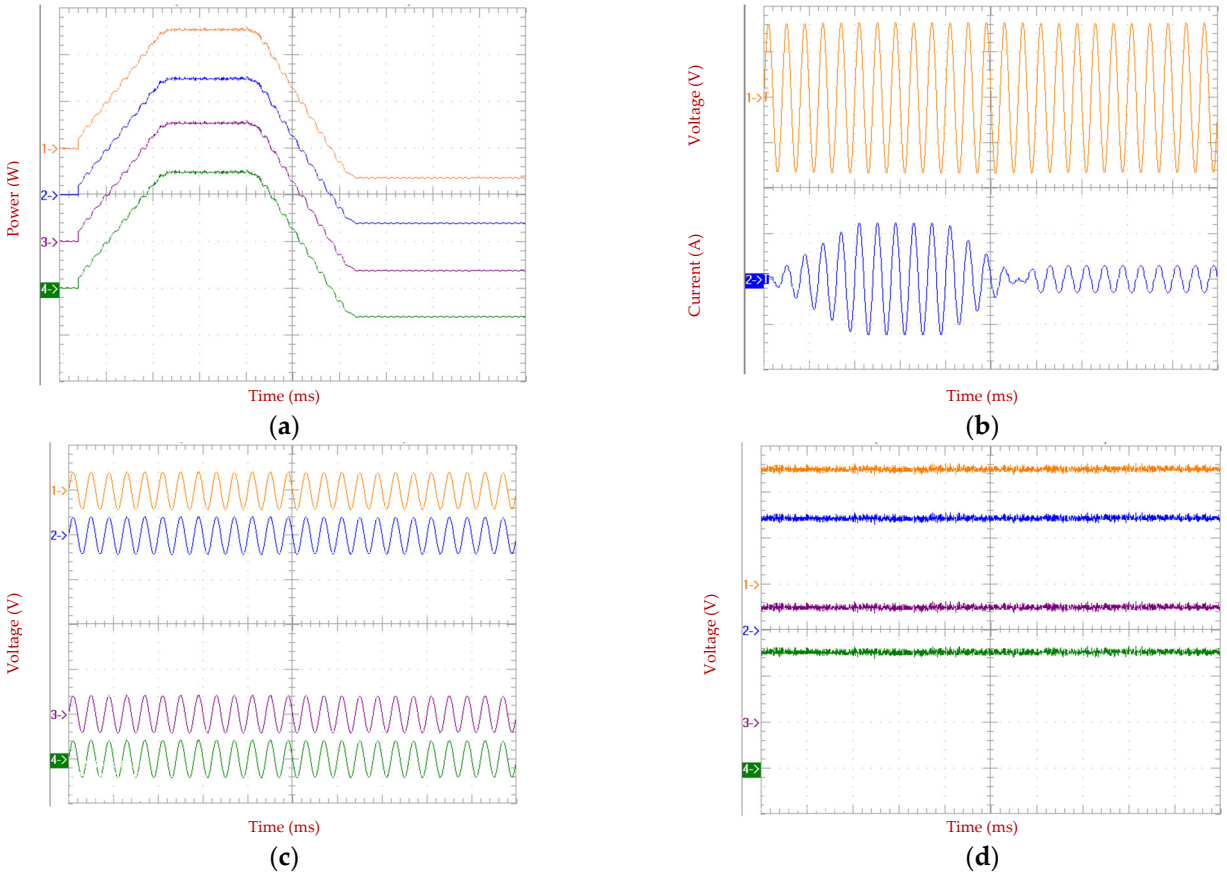


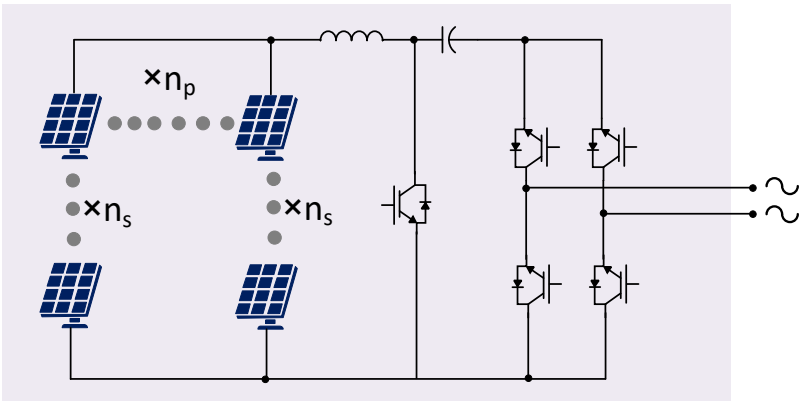
Figure 22. Experimental results of the MIs for battery/grid discharging and charging. (**a**) Powers: top (Ch1 and Ch2), MI_1 and MI_2; bottom (Ch3 and Ch4), MI_3 and MI_4; 50 ms/div–100 W/div. (**b**) Top (Ch1), grid voltage at PCC; bottom (Ch2), grid current; 50 ms/div–200 V/div–5 A/div. (**c**) Output voltages: top (Ch1 and Ch2), MI_1 and MI_2; bottom (Ch3 and Ch4), MI_3 and MI_4; 50 ms/div–200 V/div. (**d**) Input (power supplies) voltages: top (Ch1 and Ch2), MI_1 and MI_2; bottom (Ch3 and Ch4), MI_3 and MI_4; 50 ms/div–20 V/div.

7. Discussion

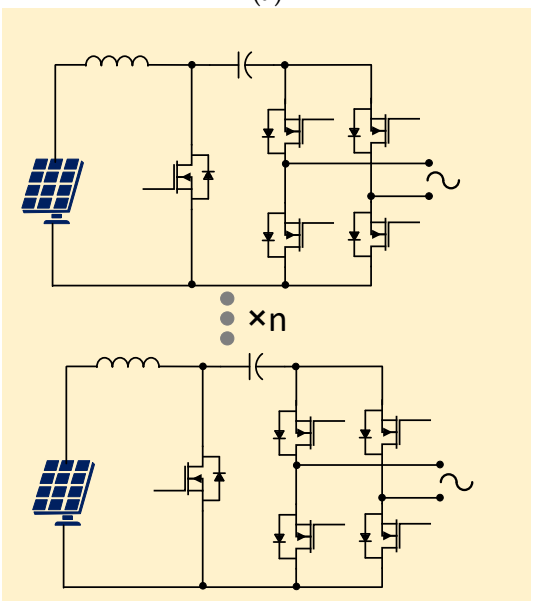
The proposed MCI offers several advantages over the conventional central inverter including improving the system performance and increasing the PV system energy harvesting. This section discusses a comparison between the Cuk central inverter and the Cuk modular inverter in terms of device stress and power losses. Figure 23 illustrates the central-based Cuk inverter versus the modular-based Cuk inverter. The number of switches used in the central Cuk inverter is five switches, while the number of switches in the modular-based Cuk inverter can be calculated as $n_t = 5n$, where n is the number of PV modules.

Figure 23a shows the PV system arrangement based on the central Cuk inverter when PV modules are connected in parallel series combination. The n_p is the number of parallel strings in the PV array, while n_s is the number of PV modules connected in series. The current rating can be calculated by multiplying the parallel string by the current at MPP. The modular Cuk inverter on Figure 23b illustrates that each PV module is connected with an independent inverter, which results in minimizing both voltage and current switches. Therefore, the size of the devices used in the design can be reduced.

The number of switches and associated power losses for both central and modular Cuk inverters are calculated according to the mathematical analysis in [25] based on the same power level of 32 kW. Tables 2 and 3 show the equations used for calculating the power losses for central-based and modular-based inverters, respectively.



(**a**)



(**b**)

Figure 23. Central versus modular Cuk inverters. (**a**) Central Cuk inverter. (**b**) Modular Cuk inverter.

Table 2. Power losses and switches stress of the central Cuk inverter.

V_{SW}	I_{SW}	Input Switch Losses	Output Switches' Losses
$V_g + n_s V_{mpp}$	$n_p I_{mpp}$	$n_p^2 r_{DS(on)} I_{mpp}^2 + \frac{3(V_g + n_s V_{mpp}) I_{mpp}}{2}\left(t_{on} + t_{off}\right) + n_p V_f I_{mpp} + n_p^2 r_{DS} I_{mpp}^2$	$r_{DS(on)} I_o^2 + \frac{(V_g + n_s V_{mpp}) I_o}{2}\left(t_{on} + t_{off}\right) + V_f I_o + r_{DS} I_o^2$

Table 3. Power losses and switch stress of the modular Cuk inverter.

V_{SW}	I_{SW}	Input Switch Losses	Output Switches' Losses
$V_g/n + n_s V_{mpp}$	$n_p I_{mpp}$	$n_p^2 r_{DS(on)} I_{mpp}^2 + \frac{n_p(V_g/n + n_s V_{mpp}) I_{mpp}}{2}\left(t_{on} + t_{off}\right) + n_p V_f I_{mpp} + n_p^2 r_{DS} I_{mpp}^2$	$r_{DS(on)} I_o^2 + \frac{(V_g/n + n_s V_{mpp}) I_o}{2}\left(t_{on} + t_{off}\right) + V_f I_o + r_{DS} I_o^2$

The number of switches used in the design will increase by increasing the number of modular Cuk inverters; however, the switches rating can be reduced, which can minimize both the cost and on-resistance of the switches. The device's stress, power losses, number of switches, and switch costs are listed in Table 4. The numerical analysis is provided for different PV module arrangements. The power losses of the modular Cuk inverter are reduced by increasing the number of modular inverts, which improve the PV system efficiency. In addition, the switch's cost drops dramatically when the modular Cuk inverter is used. Low-internal-resistance MOSFET switches can be used instead of using conventional IGBT switches. As a result, the cost can be reduced and the efficiency can be further improved. Nevertheless, when the number of switches increases significantly, the efficiency will reduce.

Table 4. Comparison between central-based and modular-based topologies at 32 kW.

Array Connection	Voltage Stress (V)	Current Stress (A)	Switches	Switch Losses (W)	Efficiency	Number of Switches	Switch Cost (GBP)
Central $n_s = 16$ $n_p = 10$	1030	136	IRG5U200SD12B IGBT	6450	≈90%	5	≈1429
Modular $n = 2$ $n_s = 8$ $n_p = 10$	515	136	IRG5U200SD12B IGBT	2560	≈92%	10	≈233
Modular $n = 4$ $n_s = 8$ $n_p = 5$	515	68	IRG5U200SD12B IGBT	1227	≈96%	20	≈167
Modular $n = 8$ $n_s = 4$ $n_p = 5$	257	68	IRG5U200SD12B IGBT	1900	≈94%	40	≈133

The modular Cuk inverter might increase the complexity of the PV system, and more switches are used in the design; however, the energy harvesting and PV system efficiency improved since each PV module can operate independently in term of MPPT during unbalanced power generation. The fault detection process can become swifter and more accurate when one of the inverters is malfunctioning.

The MPPT algorithm is not in the scope of this paper; therefore, the values for PV modules will be assumed in the look-up table, and the current of the PV module will be changed according to the voltage of the same module. Under the partial shading effect, the DSP will calculate the voltages of the PV module, and then it will assume that the MPP is changed to a new MPP value with its corresponding current.

8. Conclusions

The paper presented a single-phase LV power converter with MIs based on the Cuk inverter with ESS. The MCI connects the PV modules to battery packs on the inputs of the employed MIs. Because it is bidirectional, each Cuk MI is suitable for supporting the AC grid with power from the PV modules as well as charging the battery packs from the AC grid when necessary. The paper presented the control schemes for different modes of operation when the Cuk MI is operating as a DC/AC inverter, AC/DC rectifier, and DC/DC converter. The controllers are designed to maintain the currents from the PV modules and battery packs constant with time, while keeping the AC side voltages and currents at the grid's frequency of 50/60 Hz. Therefore, the second-order harmonic components generated by the single-phase operation are captured within the MI passive elements and decoupled from the PV module. This will improve the PV efficiency by more than 50%. The proposed

MCI is designed to mitigate mismatch problems at the PV module level, and both the conversion efficiency and the MPPT algorithm accuracy can be improved. The bidirectional power flow of the MCI enables connecting battery packs in parallel with the PV module. In this way, the harvested energy can be stored during light loading instead of shedding the PV power. The experimental results of the 1 kW prototype presented the feasibility of MCI with PV modules as well as battery packs using four MIs when connected to the full grid voltage. The experimental results have demonstrated the ability of the proposed system to extract the maximum available power from the PV modules during either normal or partial shading conditions. The paper has not discussed the design and operation of the employed HFT in the Cuk MIs as well as the full MPPT system, and this will be considered in a future work.

Author Contributions: Conceptualization, A.D.; Methodology, Y.A. and A.D.; Software, Y.A.; Validation, Y.A.; Formal analysis, Y.A. and A.D.; Investigation, Y.A. and A.D.; Data curation, A.D.; Writing—original draft, Y.A. and A.D.; Writing—review & editing, A.D.; Visualization, Y.A. and A.D.; Supervision, A.D.; Project administration, A.D. All authors have read and agreed to the published version of the manuscript.

Funding: This research received no external funding.

Data Availability Statement: Not applicable.

Conflicts of Interest: The authors declare no conflict of interest.

References

1. IREA. Renewable Power Generation Costs in 2020. 2020. Available online: https://www.irena.org/publications/2021/Jun/Renewable-Power-Costs-in-2020 (accessed on 22 February 2023).
2. Qin, S.; Barth, C.B.; Pilawa-Podgurski, R.C.N. Enhancing Microinverter Energy Capture with Submodule Differential Power Processing. *IEEE Trans. Power Electron.* **2016**, *31*, 3575–3585. [CrossRef]
3. Yang, B.; Zhu, T.; Wang, J.; Shu, H.; Yu, T.; Zhang, X.; Yao, W.; Sun, L. Comprehensive overview of maximum power point tracking algorithms of PV systems under partial shading condition. *J. Clean. Prod.* **2020**, *268*, 121983. [CrossRef]
4. Lin, L.; Zhang, J.; Deng, Y. Differential Power Processing Architecture with virtual port in series and MPPT in submodule level. In Proceedings of the 2019 IEEE Energy Conversion Congress and Exposition (ECCE), Baltimore, MD, USA, 29 September–3 October 2019.
5. de Abreu Mateus, T.H.; Pomilio, J.A.; Godoy, R.B.; Pinto, J.O. Distributed MPPT scheme for grid connected operation of photovoltaic system using cascaded H-bridge multilevel converter under partial shading. In Proceedings of the 2017 IEEE Southern Power Electronics Conference (SPEC), Puerto Varas, Chile, 4–7 December 2017.
6. Ramos-Paja, C.A.; Petrone, G.; Spagnuolo, G.; Gonzalez, D.; Sergio-Serna, S. Current equalization of mismatched PV panels based on a capacitor energy storage. In Proceedings of the 2018 IEEE International Conference on Industrial Technology (ICIT), Lyon, France, 20–22 February 2018.
7. Uno, M.; Shinohara, T. Module-integrated converter based on cascaded quasi-Z-source inverter with differential power processing capability for photovoltaic panels under partial shading. *IEEE Trans. Power Electron.* **2019**, *34*, 11553–11565. [CrossRef]
8. Marti-Arbona, E.; Mandal, D.; Bakkaloglu, B.; Kiaei, S. PV panel power optimization using sub-panel MPPT. In Proceedings of the 2015 IEEE Applied Power Electronics Conference and Exposition (APEC), Charlotte, NC, USA, 15–19 March 2015.
9. Mohanty, P.; Muneer, T.; Kolhe, M. *Solar Photovoltaic System Applications—A Guidebook for Off-Grid Electrification*; Springer: Cham, Switzerland, 2016.
10. Robles, H.R.; Azuaje, B.J.; Scheller, C.J.; Angulo, A.; Mancilla, F. Detailed modeling of large scale photovoltaic power plants under partial shading conditions. *Sol. Energy* **2019**, *194*, 485–498. [CrossRef]
11. Pilawa-Podgurski, R.C.; Perreault, D.J. Submodule Integrated Distributed Maximum Power Point Tracking for solar photovoltaic applications. *IEEE Trans. Power Electron.* **2013**, *28*, 2957–2967. [CrossRef]
12. Bastidas-Rodriguez, J.D.; Franco, E.; Petrone, G.; Ramos-Paja, C.A.; Spagnuolo, G. Maximum power point tracking architectures for photovoltaic systems in mismatching conditions: A Review. *IET Power Electron.* **2014**, *7*, 1396–1413. [CrossRef]
13. Zhang, F.; Xie, Y.; Hu, Y.; Chen, G.; Wang, X. A hybrid boost-flyback/flyback microinverter for photovoltaic applications. *IEEE Trans. Ind. Electron.* **2020**, *67*, 308–318. [CrossRef]
14. Chiu, H.-J.; Lo, Y.-K.; Yang, C.-Y.; Cheng, S.-J.; Huang, C.-M.; Chuang, C.-C.; Kuo, M.-C.; Huang, Y.-M.; Jean, Y.-B.; Huang, Y.-C. A module-integrated isolated Solar Microinverter. *IEEE Trans. Ind. Electron.* **2013**, *60*, 781–788. [CrossRef]
15. Leuenberger, D.; Biela, J. PV-module-integrated AC inverters (AC modules) with subpanel MPP tracking. *IEEE Trans. Power Electron.* **2017**, *32*, 6105–6118. [CrossRef]

16. Gagrica, O.; Nguyen, P.H.; Kling, W.L.; Uhl, T. Microinverter curtailment strategy for increasing photovoltaic penetration in low-voltage networks. *IEEE Trans. Sustain. Energy* **2015**, *6*, 369–379. [CrossRef]
17. Nuotio, M.; Ilic, M.; Liu, Y.; Bonanno, J.; Verlinden, P.J. Innovative AC photovoltaic module system using series connection and universal low-voltage micro inverters. In Proceedings of the 2014 IEEE 40th Photovoltaic Specialist Conference (PVSC), Denver, CO, USA, 8–13 June 2014.
18. Ali, A.I.M.; Tuan, C.A.; Takeshita, T.; Sayed, M.A.; Alaas, Z.M. Modular Single-Stage Three-Phase Flyback Differential Inverter for Medium/High-Power Grid Integrated Applications. *Sensors* **2022**, *22*, 2064. [CrossRef] [PubMed]
19. Ahmed, S.; Takeshita, T.; Sayed, M. Single-stage three-phase grid-tied isolated SEPIC-based differential inverter with improved control and selective harmonic compensation. *IEEE Access* **2020**, *8*, 147407–147421.
20. Xiao, B.; Hang, L.; Mei, J.; Riley, C.; Tolbert, L.M.; Ozpineci, B. Modular Cascaded H-Bridge Multilevel PV Inverter with Distributed MPPT for Grid-Connected Applications. *IEEE Trans. Ind. Appl.* **2015**, *51*, 1722–1731. [CrossRef]
21. Darwish, A.; Alotaibi, S.; Elgenedy, M.A. Current-source Single-phase Module Integrated Inverters for PV Grid-connected Applications. *IEEE Access* **2020**, *8*, 53082–53096. [CrossRef]
22. Darwish, A.; Elserougi, A.; Abdel-Khalik, A.S.; Ahmed, S.; Massoud, A.; Holliday, D.; Williams, B.W. A single-stage three-phase DC/AC inverter based on Cuk converter for PV application. In Proceedings of the 7th GCC Conference and Exhibition (GCC), Doha, Qatar, 17–20 November 2013; pp. 384–389.
23. Badawy, A. D Current Source DC-DC and DC-AC Converters with Continuous Energy Flow. Ph.D. Thesis, University of Strathclyde, Glasgow, UK, 2015.
24. Alotaibi, S.; Darwish, A. Modular Multilevel Converters for Large-Scale Grid-Connected Photovoltaic Systems: A Review. *Energies* **2021**, *14*, 6213. [CrossRef]
25. Rafiq, U.; Murtaza, A.F.; Sher, H.A.; Gandini, D. Design and Analysis of a Novel High-Gain DC-DC Boost Converter with Low Component Count. *Electronics* **2021**, *10*, 1761. [CrossRef]

Disclaimer/Publisher's Note: The statements, opinions and data contained in all publications are solely those of the individual author(s) and contributor(s) and not of MDPI and/or the editor(s). MDPI and/or the editor(s) disclaim responsibility for any injury to people or property resulting from any ideas, methods, instructions or products referred to in the content.